Dual Extraction of Photogenerated Electrons and Holes from a Ferroelectric $Sr_{0.5}Ba_{0.5}Nb_2O_6$ Semiconductor

Dayong Fan,[†,‡] Jian Zhu,[†,‡] Xiuli Wang,[†] Shengyang Wang,[†,‡] Yong Liu,[†,‡] Ruotian Chen,[†,‡] Zhaochi Feng,[†] Fengtao Fan,[*,†] Can Li[*,†]

†State Key Laboratory of Catalysis, Dalian Institute of Chemical Physics, Chinese Academy of Sciences; Dalian National Laboratory for Clean Energy, Dalian 116023, China

‡Graduate University of Chinese Academy of Sciences, Beijing 100049, China.

Corresponding Authors: E-mail[*]: canli@dicp.ac.cn.

E-mail[*]: ftfan@dicp.ac.cn.
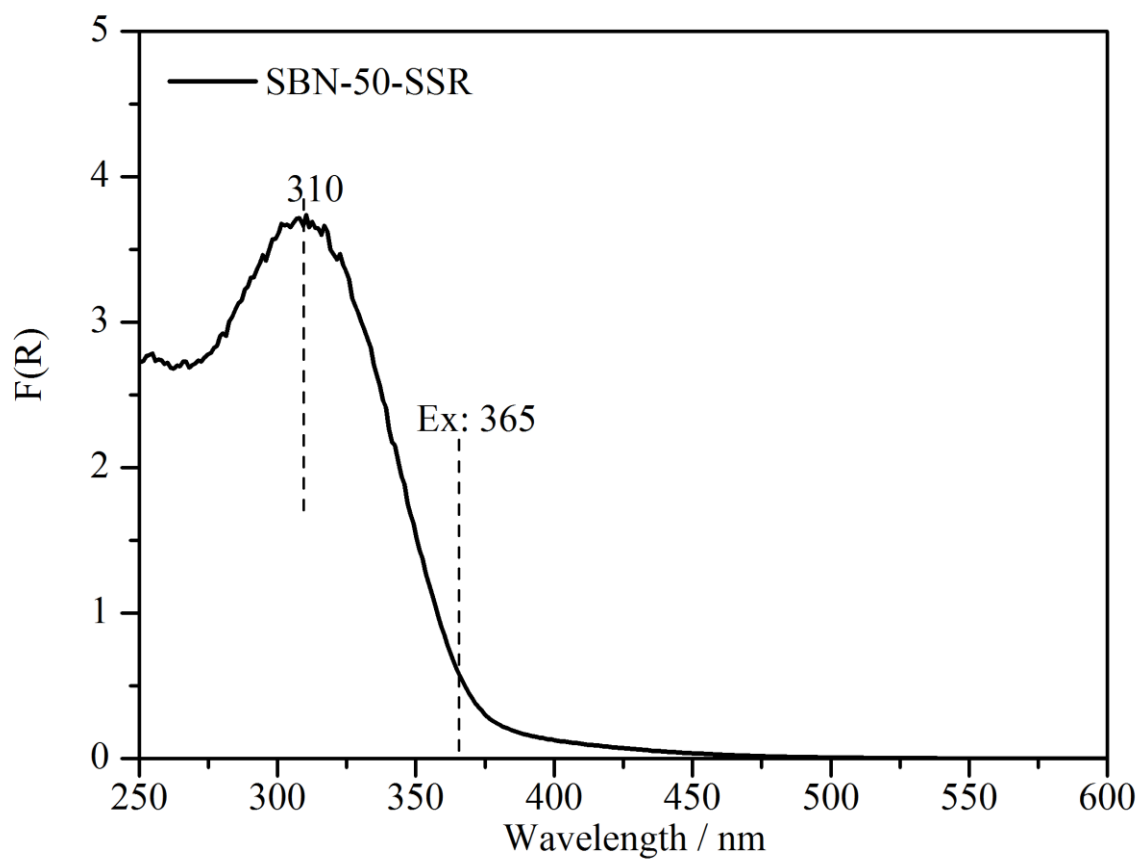
UV-visible absorption spectroscopy measurement

Fig. S1 Ultraviolet–visible diffuse reflectance spectra of SBN-50-SSR powder taken F(R) as Y axis,

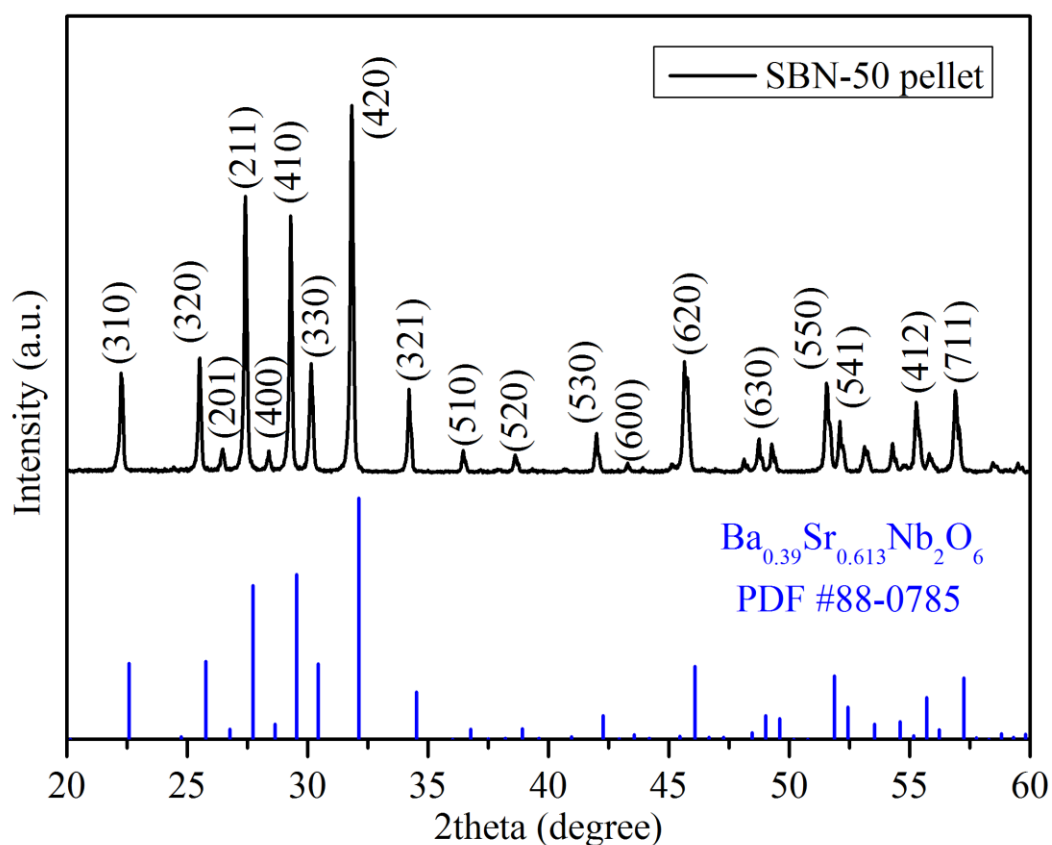where F(R) is the Kubelka–Munk function of the diffuse reflectance calculated by $F(R)=(1-R)^2/2R$

Fig. S2 X-ray powder diffraction pattern of sintered SBN-50 pellet, which matches well with the standard JCPDS #88-0785 tetragonal tungsten bronze SBN structure, no second phase appears.

Table S1. The atom ratios (Sr, Ba) relative to Nb in the sintered SBN-50 pellet, was measured by ICP-OES (Inductively Coupled Plasma Optical Emission Spectrometry) method:

	Sr	Ba	Nb
No. 1[a]	0.4837 ± 0.0286	0.5418 ± 0.0892	2
No. 2[a]	0.4847 ± 0.0083	0.5349 ± 0.0015	2

[a] *Before microwave digestion, the ceramic was crushed and ground. Two times measurements are performed.*
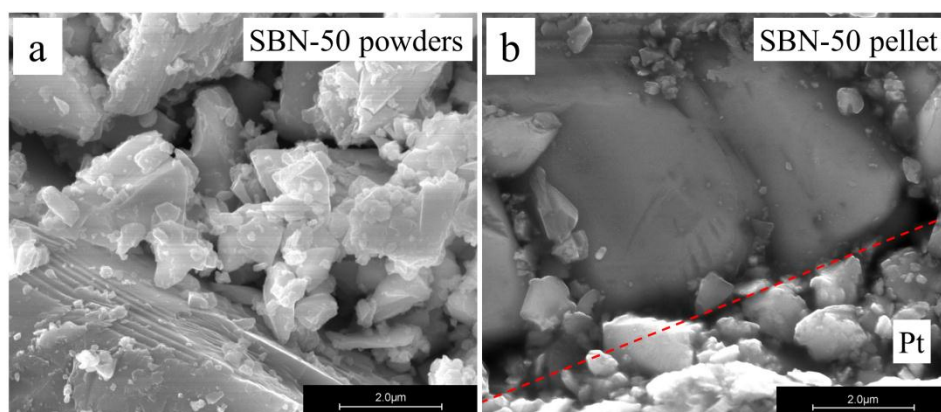
Figure S3. SEM photograghs of SBN-50 powders (a) and SBN-50/Pt interface (b)
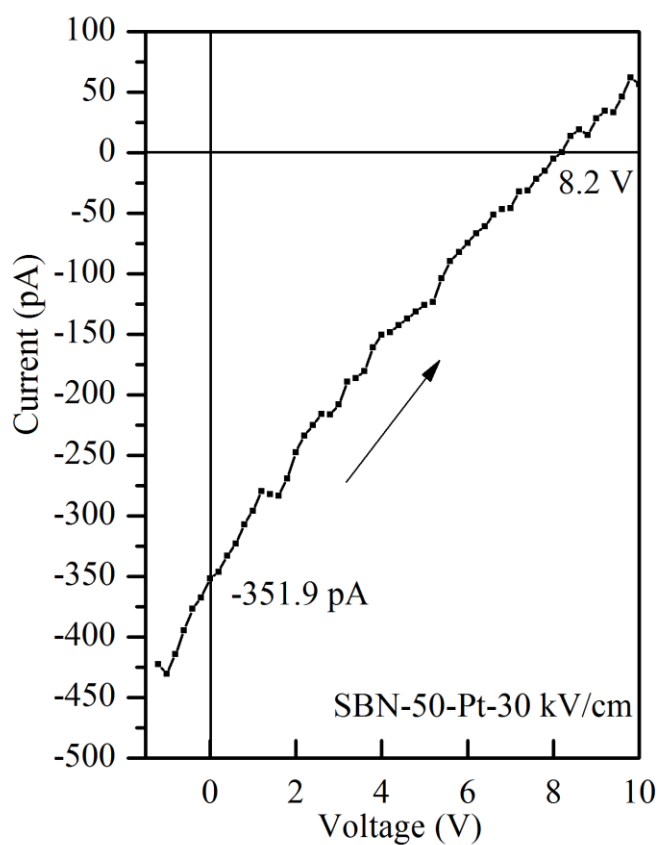

Fig. S4 I-V curves under 365 nm LED illumination: the poled SBN-50 with symmetrical Pt electrodes. The curve corresponding to the first time scan after poling with E=30 kV/cm for 30mins, which shows V_{oc} was as high as 8.2 V and I_{sc} was -351.9 pA. The arrow in the figure indicate the scanning direction.

Photoelectric test method reliablity and APV effect stability of SBN

For the large impedance of the SBN-50 pellets, it is hard to measure the DC current correctly. The high RC time constant and the high additional displacement current always induce large deviation from the real DC current. Here, using the voltage sweep method, data acquisition with long holding time (10s) for each point was adopted to avoid the disturbance of the displacement current. Besides, the long holding time (10s) ensures the collected data are after the dielectric relaxation of the capacitor. This is demonstrated by overlap of the forward sweep and backward sweep(see Fig. S5). Forward scan: from negative voltage to positive voltage.
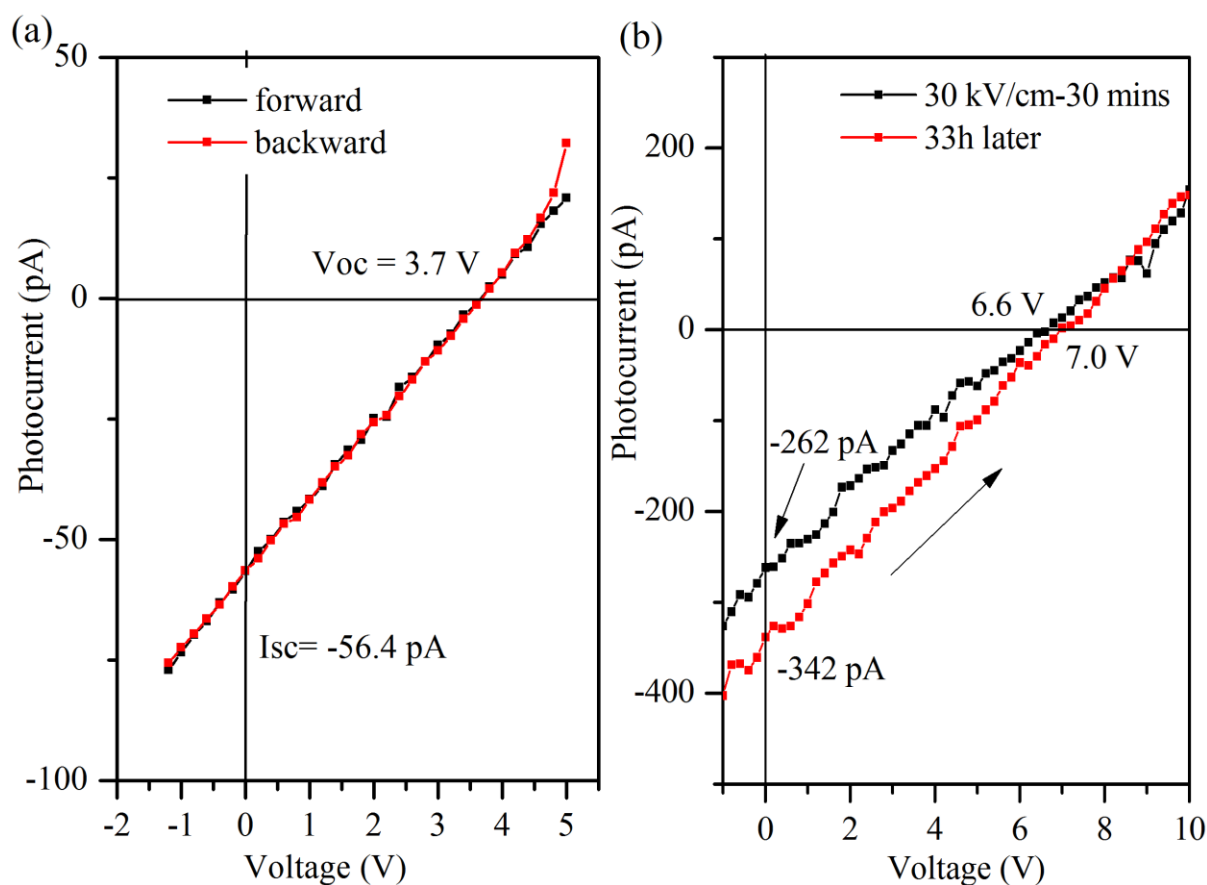

Fig. S5 (a) I-V curves under 365nm LED illumination: SBN-50-Pt sample poled with 10 kV/cm for 30 mins. The forward sweep result (black) coincides with the backward one (red). (b) The PV output of SBN-50-Pt poled with E= 30 kV/cm remained stable even after the sample had been perserved under ambient condition for 33 hours.

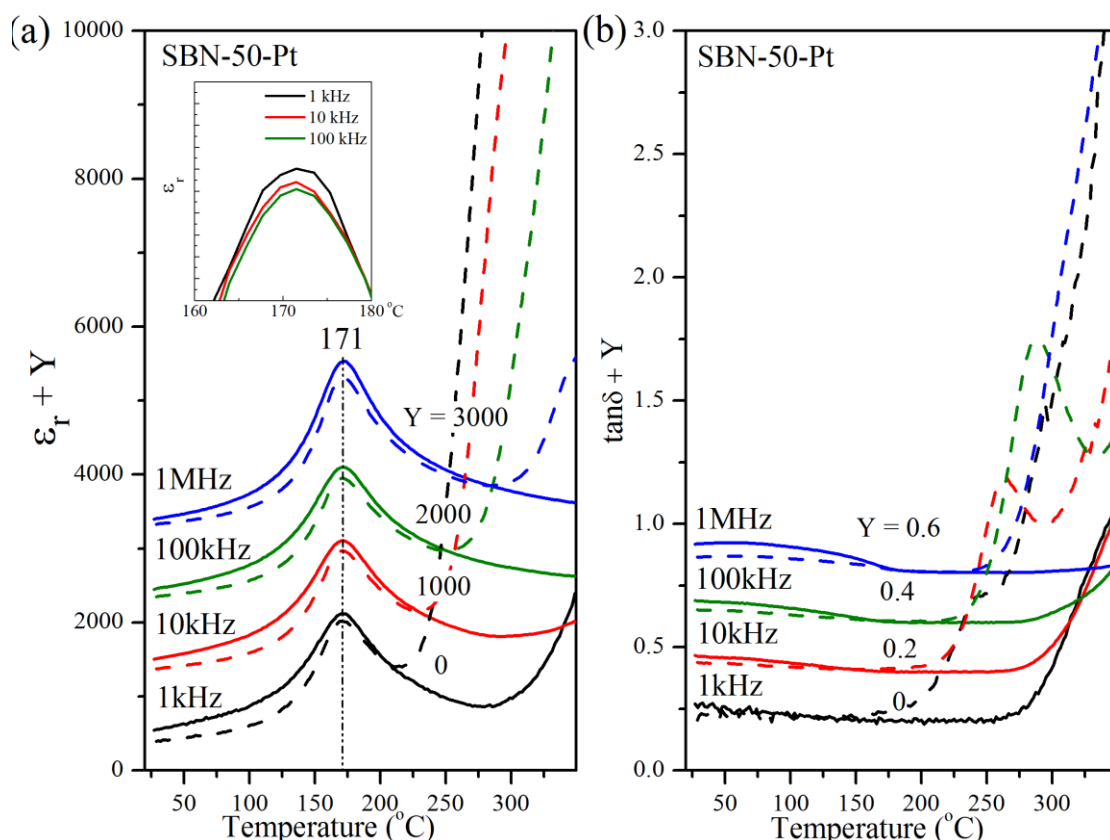**Fig. S6** The temperature dependence of (a) dielectric constant (ε_r) and (b) dielectric loss (tanδ) at 1 kHz, 10 kHz, 100 kHz, 1 MHz of SBN-50-Pt. (solid line: As-grown sample; dashed line: after poled with E=30 kV/cm. The dielectric constants and dielectric loss were modified by adding certain increments (Y) to well reflect the influence of the poling effect. Insert in (a): the unmodified dielectric constant.

An abnormal increment of dielectric constant is shown in Fig. S6. The onset temperature is different with various frequencies: 210^oC (1 kHz), 230^oC (10 kHz), 250^oC (100 kHz), 300^oC (1 MHz). Accordingly, the dielectric losses (tanδ) also increase rapidly on the corresponding temperature by poling. The similar abnormal increment is also observed in poled SBN-50-Ag.

Oxygen vacancies exist widely in the high-temperature calcined oxides and have a great impact on the ferroelectric behaviors, such as hopping conduction. From the literature, it has been shown that with increasing temperature, an abnormally rapid increase of ε and tanδ in Bi:$SrTiO_3$ happened from 220^oC to 400^oC and was attibuted to the short-range motion of the doubly oxygen vacanices. These dielectric behaviors resemble that of SBN-Pt pellet after poling. Thus, we attribute the abnormal increment of ε and tanδ to the production of doubly ionized oxygen vacancies due to the high electric field. Two kinds of

oxygen vacancies are usually formed: the singly ionized one and the douly one. The former has the ionization energy of 0.1 eV, while the latter has the ionization energy which is much larger (1.4 eV). An electrode reaction at the anode may happen under the high electric field strength, and consequently result in the production of doubly ionized oxygen vacancies.

Inevitably, the space charge region formed by the inhomogeneous distribution of oxygen vacancies maybe the origin of the leaky P-E loop. This process induces the saturated V_{oc} on high electric field poling (ca. 30 kV/cm), as shown in Fig. S7.
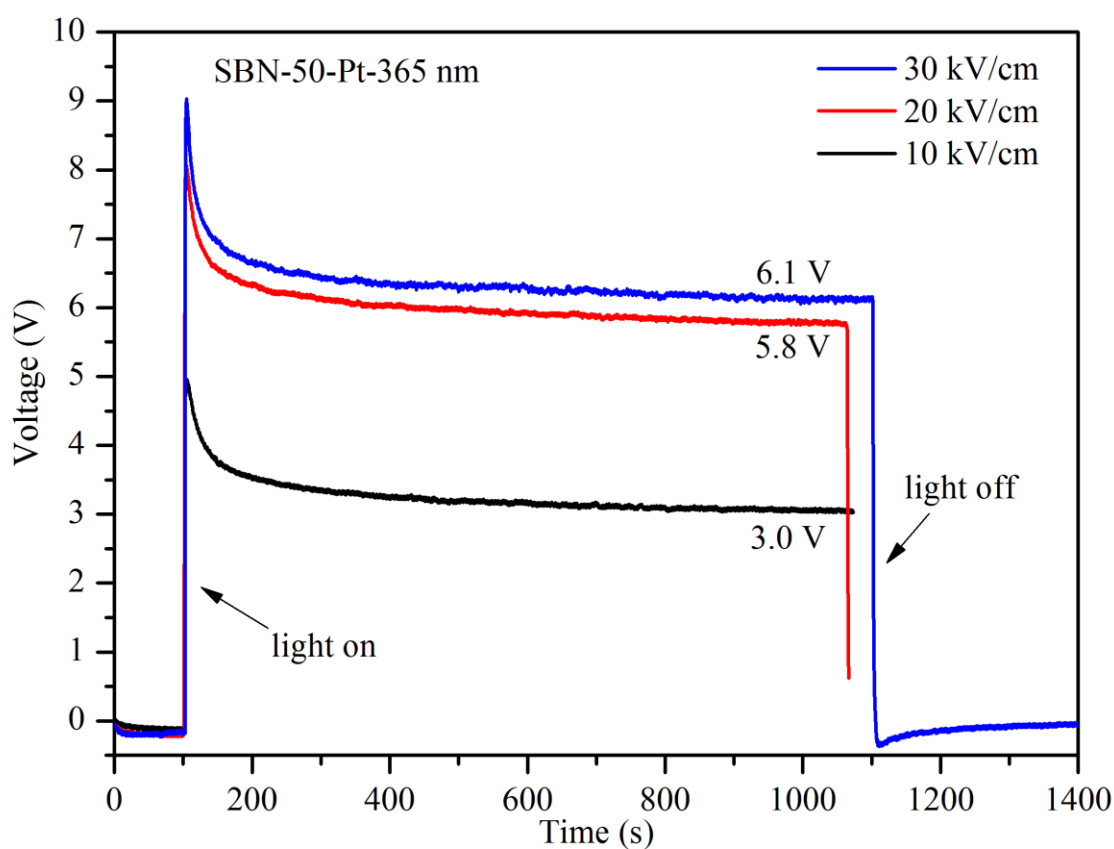

Fig. S7 Ferroelectric photovoltaic effect of SBN-50-Pt pellet poled with different electrical fields under open circuit conditions, excited with 365 nm LED light source.

Photoelectrochemical test for flat-band position calculation

The flat-band position (ϕ_{fb}) of unpoled SBN-50 can be inferred from Mott-Schottky relation:

$$\frac{1}{C_{sc}^2} = \frac{2}{N_d e \varepsilon_o \varepsilon_r}\left(\phi - \phi_{fb} - \frac{k_b T}{e}\right)$$

which is equal to the intercept of the M-S plots (Figure 4a). The flat band ϕ(NHE) can be converted to ϕ(AVS) from the relationship:

$$\phi(AVS) = \phi(NHE) + 0.0591 \times pH + 4.44 \text{ (eV) at } 25°C$$
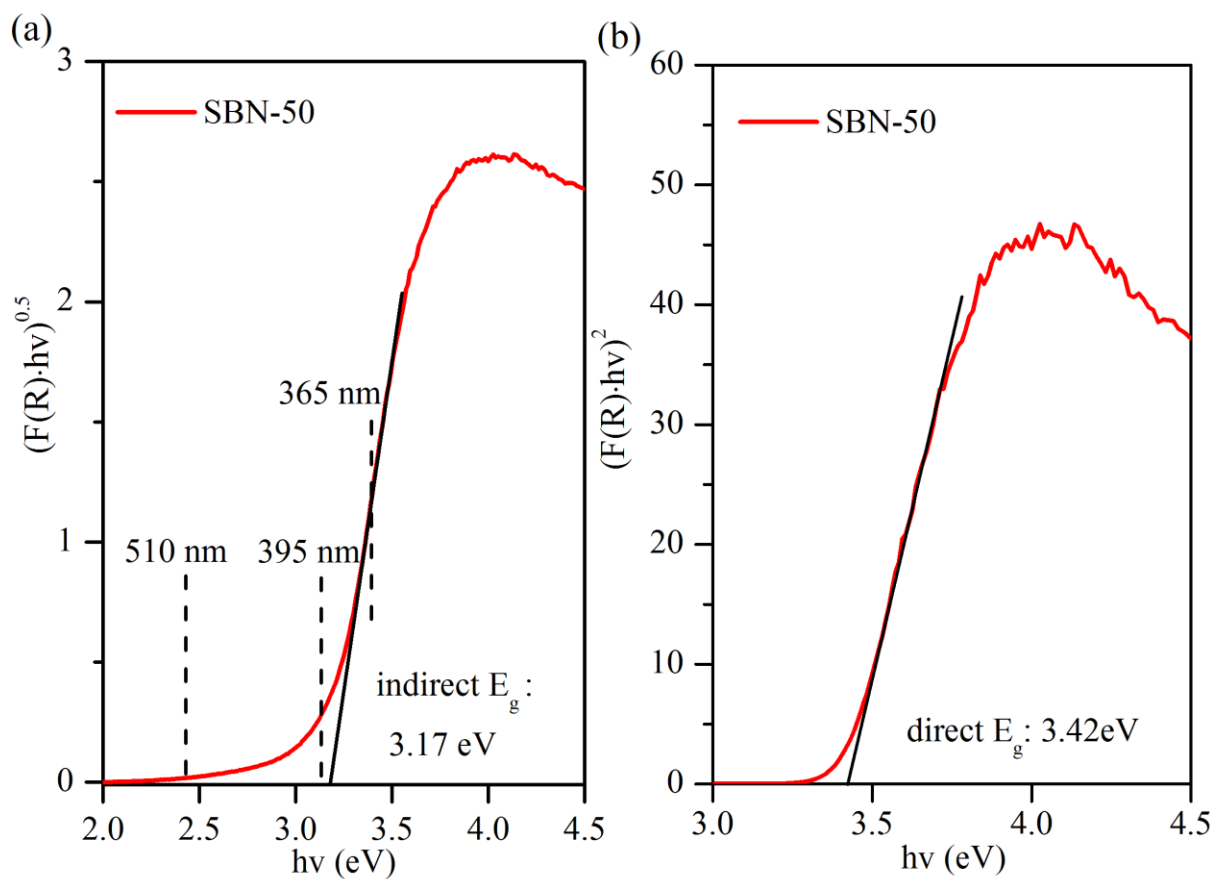

Fig. S8 Tauc plots of SBN-50-SSR powder: (a) indirect and (b) direct band gap analysis.

Photocatalysis characterization

SBN-50 is in ferroelectric phase at RT and its H_2-evolving photocatalysis activity was very low (30 µmol/g for 2 hours) even with methanol as the electron donor. After the Pt loading (1wt%) as the cocatalyst, a strongly enhanced activity was detected (416 µmol/g for 2h).
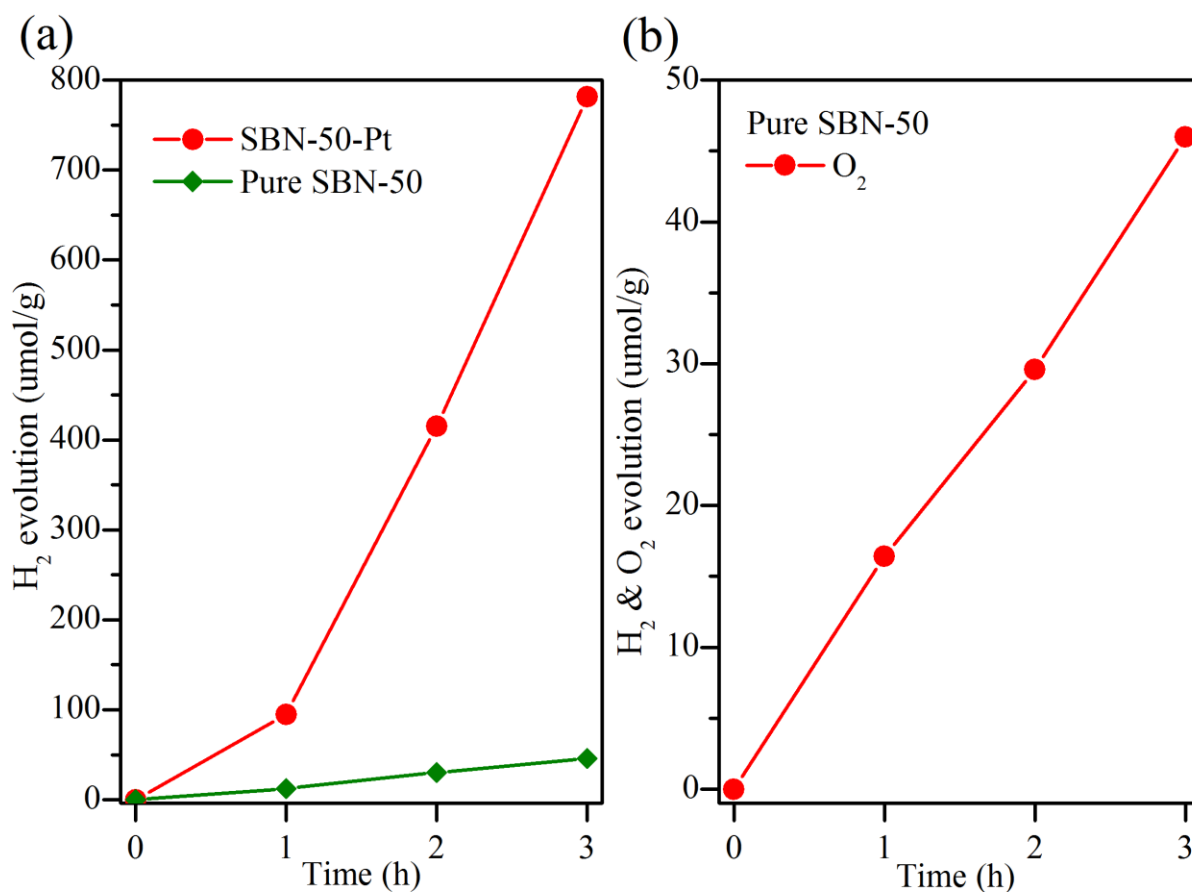

Fig. S9 (a) Reaction conditions: 0.05 g photocatalyst loaded with 1.0 wt% Pt cocatalyst by in-situ photodeposition method; aqueous 10 vol% CH_3OH solution (100 mL); quartz top-irradiation type; 300 W Xe lamp (Cermax:PE300BUV); (b) O_2 evolution from aqueous 10 mM $FeCl_3$ solution (100 mL)
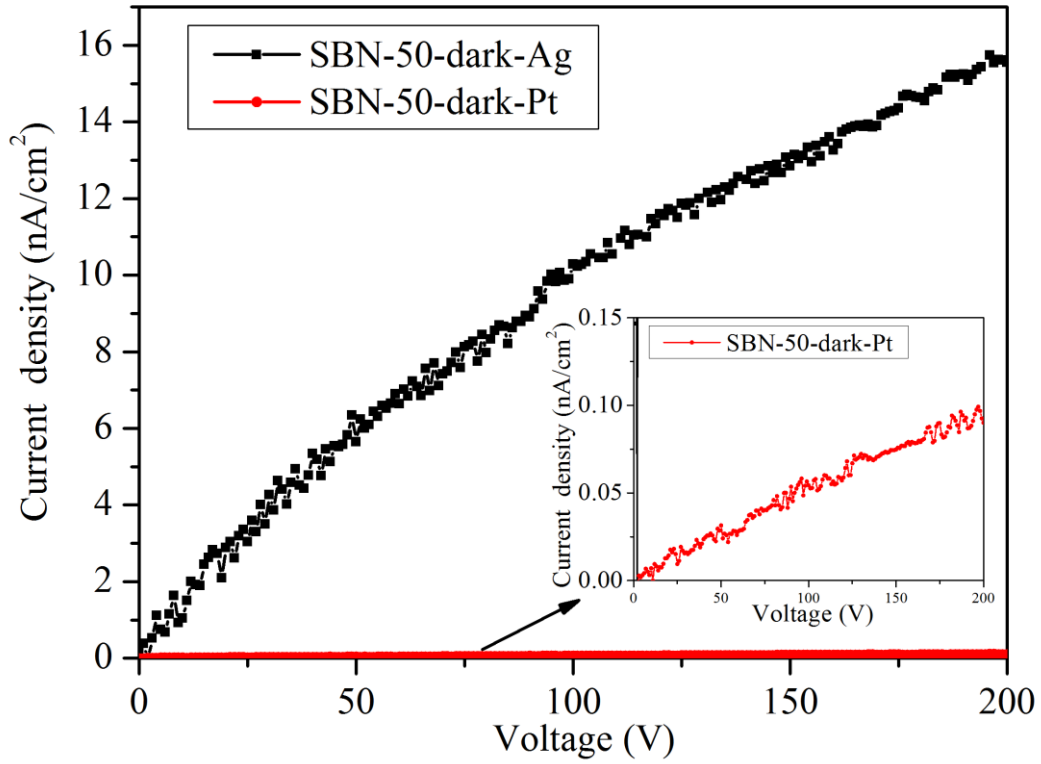
Fig. S10 I-V curves of SBN-Pt and SBN-Ag in dark

Debye screening length calculation and the SCR width of Schottky barriers (w_0)

From the slope of the $1/C_{sc}^2$ vs. E in Fig 4, the positive values indicate that the majority carrier of SBN-50 is electron, which is consistent with the fact that only the photo-oxidation reaction on the SBN-50 electrode was observed, and N_d was estimated from

$$K=\frac{2}{N_d e \varepsilon_o \varepsilon_r}$$

to be 4.51×10^{19} cm^{-3}.(The relative permittivity ε_r(1000 Hz, RT) = 522.2 is from $1/C_{sc}^2$ curve of SBN-50 pressed pellet.)

So the Debye screening length(L_D) can be estimated by:

$$L_D=\sqrt{\frac{kT\varepsilon_r\varepsilon_0}{e^2 N_d}}$$

where e =1.6×10^{-19} C. We get $L_D \approx 3.8$ nm.

The SCR width of Schottky barriers (w_0) on Pt-SBN-50 interfaces(V_s = 1.14 V):

$$w_0=L_D \cdot \sqrt{\frac{2qV_s}{kT}} \approx 38 \text{ nm}$$

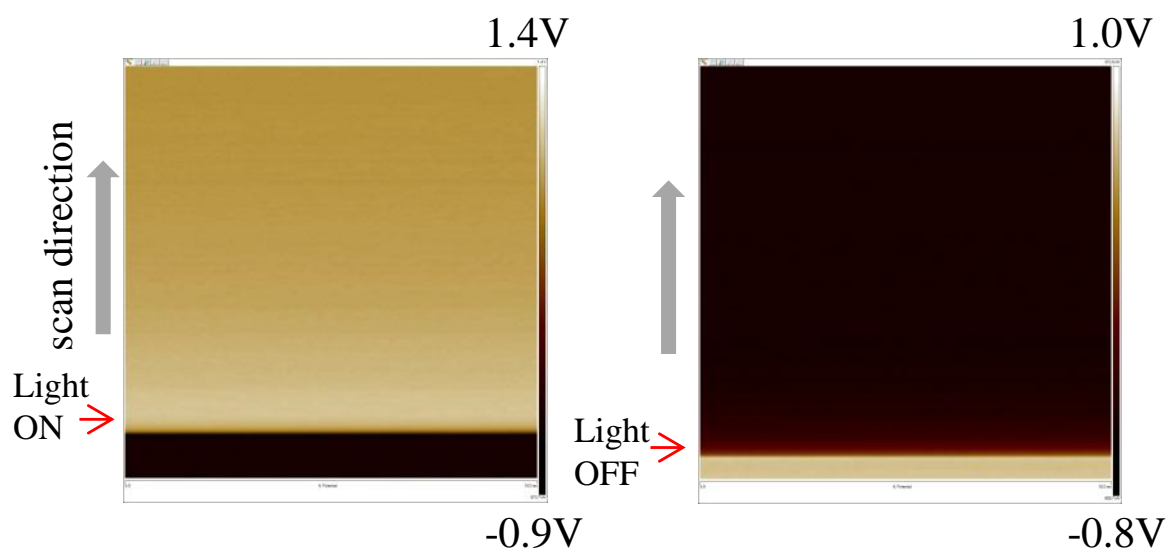**Fig. S11.** KPFM images of positive poled Pt$^+$ with LED 365nm illumination after SBN-50-Pt was poled with E=30 kV/cm
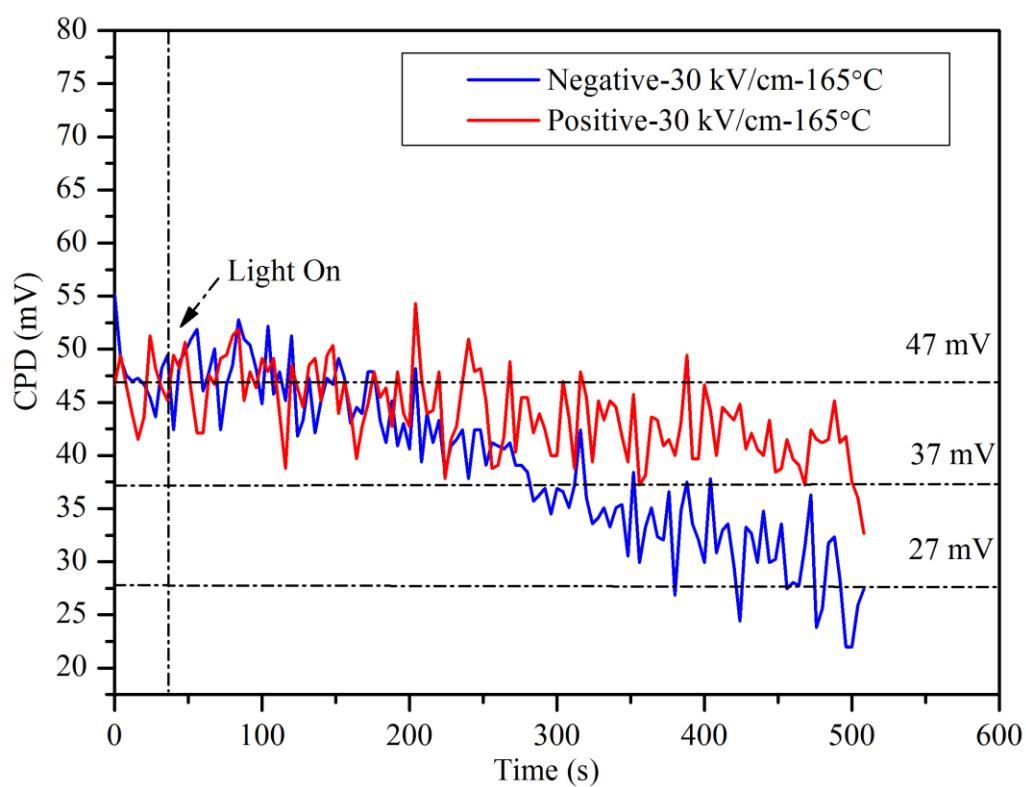

Fig. S12. The time dependent CPD profiles on two poled Ag electrodes with UV illumination on thermal depoled SBN-Ag